Physica B 639 (2022) 414025

Contents lists available at ScienceDirect

Physica B: Physics of Condensed Matter

journal homepage: www.elsevier.com/locate/physb

Investigation on optical Tamm states based on graphene-dielectric cylindrical photonic crystals

Jia-Tao Zhang [a], Si-Si Rao [a], Dan Zhang [b], Hai-Feng Zhang [a,*]

[a] College of Electronic and Optical Engineering & College of Flexible Electronics, Nanjing University of Posts and Telecommunications, Nanjing, 210023, China
[b] College of Information Science and Technology, Nanjing Forestry University, Nanjing, 210037, China

ARTICLE INFO

Keywords:
Cylindrical photonic crystals
Optical Tamm state
Graphene
Transfer matrix method

ABSTRACT

In this paper, the principle of the transfer matrix method (TMM) is applied to derive the dispersion relation of electromagnetic wave propagation in cylindrical photonic crystals (CPCs), and we further deduce the conditional equations for exciting the optical Tamm state (OTS) in the one-dimensional (1D) CPCs based on the excitation conditions for OTS in 1D photonic crystals. Both H- and E-polarization are involved. After that, four CPCs are designed with graphene as the main defect layer to verify the correctness of the formula, and the effects of different defect layer structures, dielectric thickness, chemical potential, and phenomenological scattering rate on the dispersion curve are discussed, separately. In contrast, differences due to defect layer structure and dielectric thickness are more easily to be observed. The chemical potential of graphene dependence on the k_ρ-ω curves is more likely to be a kind of positive correlation. While phenomenological scattering rate has the weakest effect on the results.

1. Introduction

For a long time, people have been studying the propagation of electromagnetic waves in dielectric layered structures. Since the two pioneering works of Yablonovitch [1] and John [2] introduced the concept of photonic crystals (PCs) [3,4], such problems once again aroused great interest in the fields of optics and electromagnetics in 1987. Since then, it led to a large number of PCs research projects in the past three and half decades. Nowadays, scholars in the fields of photonics [5], electronics [6], and materials physics [7] continue to take photonic crystals as a hot spot of research.

A simple multilayer structure formed by alternating dielectrics periodically is called one-dimensional (1D) PCs, which are easier to prepare than 2D and 3D PCs. Moreover, because of the transfer matrix method (TMM) [8], we can explore the transmission characteristics of electromagnetic waves in the 1D PCs more conveniently. However, in comparison, the cylindrical photonic crystals (CPCs) [9–12] are more abundantly used in reality. By extending the TMM in the 1D PCs to the cylindrical coordinate system, the transmission properties of columnar waves in CPCs can be easily calculated [13–16], which makes the columnar periodic dielectric structure widely used in a variety of active and passive optoelectronic devices, including sensors [17], laser light sources [18], modulators [19], etc. In recent years, this structure has continued to be the focus of attention for many scholars. In 2017, Egypt researchers El-Naggar et al. [20] explored the electromagnetic wave propagation properties in the CPCs incorporating a single negative material and investigated the three gaps of zero-phase, zero-permittivity, and zero-permeability. A wide-bandgap CPCs structure with polarization-independent characteristics at high azimuthal modulus was proposed by them. In the same year, Ukrainian scholars Averkov et al. [21] theoretically analyzed the dispersion properties of anisotropic cylindrical solid waveguide intrinsic waves without dispersion of the dielectric constant tensor components. The research on CPCs is bound to continue.

In addition, the optical Tamm state (OTS) [22–25] is also one of the focuses of interest in this paper, which is a non-dissipative interface mode localized at the boundary of two different medium structures. Since Kavokin [26] first proposed the concept of OTS in 2005, it has caused extensive research by a large number of scholars and scientific research teams. Because of the requirements of local field enhancement, surface limitation, etc., OTS itself is widely used in the fields of nonlinear optics, light modulators, and sensors. Commonly, 1D PCs

* Corresponding author. College of Electronic and Optical Engineering & College of Flexible Electronics, Nanjing University of Posts and Telecommunications, Nanjing, 210023, China.
E-mail address: hanlor@163.com (H.-F. Zhang).

https://doi.org/10.1016/j.physb.2022.414025
Received 4 March 2022; Received in revised form 23 April 2022; Accepted 15 May 2022
Available online 20 May 2022
0921-4526/© 2022 Elsevier B.V. All rights reserved.

heterostructures or metal-distributed Bragg mirrors are frequently used to observe OTS. And with the rise of 2D materials represented by graphene and black phosphorus, there are more options for the excitation of OTS. Especially, graphene [27–29], with its numerous excellent optoelectronic properties, when introduced as a defect, can make the excitation of OTS independent of the polarization direction of the incident wave, in addition, even vertically incident electromagnetic waves can excite OTS. As early as 2010, Jiang et al. [30] have investigated the Tamm state localized at the interface between graphene superlattices and homogeneous graphene. In this paper, we also use graphene as the defect to excite OTS in the CPCs. It is worth mentioning that because of its excellent characteristics, graphene has received extensive attention not only in optics but also in materials science [31], chemistry [32], condensed matter physics [33], and other fields.

In this paper, we derive the formulas of the conditions for excitation of OTS in the CPCs and propose several simple graphene doping structures to attempt the adjustment of dispersion curves by changing various parameters. The simulation results demonstrate that the effects of defect layer structure and dielectric thickness on the dispersion curve is more obvious, with a maximum difference of 0.0248(2πc/d) and 0.0171(2πc/d) in angular frequency ω for the same ρ-directional component of the wave vector k_ρ. At the same time, regulating thickness of each dielectric layers in the CPCs structure can also cause the difference between the passband and forbidden band distribution. In contrast, the alteration caused by chemical potential μ_C and the phenomenological scattering rate of graphene τ are not significant.

2. Structure design and simulation

As shown in Fig. 1, the CPCs investigated in this paper are consisted of a graphene layer and dielectric layers, whose thicknesses can be denoted by d_G, d_0, d_A, and d_B, respectively, with an initial radius ρ_{-1}. The graphene layer appears as the black part in the diagram, while A, B, and C are three dielectrics with different refractive indexes of n_A, n_B, and n_0, where $n_0 = 1$. In this structure, the graphene layer G and the dielectric $(C)(AB)^N$ are distributed from the center outward, where N represents the number of periods.

We start with the two curl equations of Maxwell's equations [13].

$$\nabla \times \mathbf{E} = -\mathrm{j}\omega\mu\mathbf{H} \tag{1}$$

$$\nabla \times \mathbf{H} = \mathrm{j}\omega\varepsilon\mathbf{E} \tag{2}$$

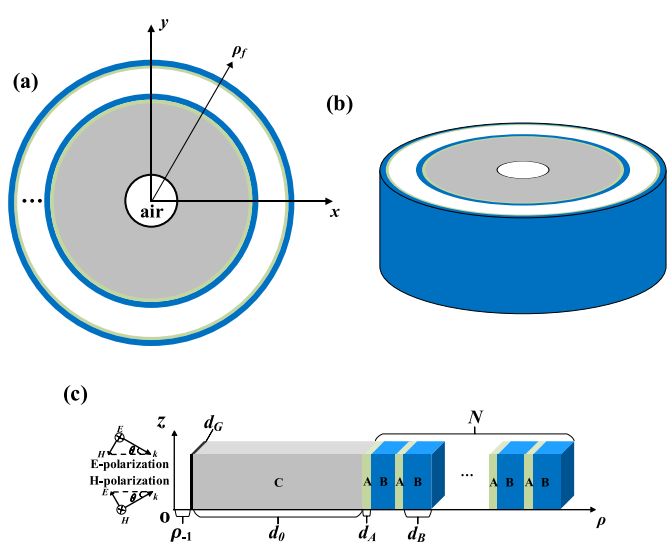

Fig. 1. The model diagram of CPCs with graphene as a defect layer, (a) Top view of the model, (b) Stereogram of the model, and (c) Sectional view of the model.

Firstly, take the example of H-polarization. Assume that the electromagnetic wave propagates along the $\boldsymbol{\rho}$ axis and its derivative to $\boldsymbol{z}$ can be omitted as 0. Expand Eqs. (1) and (2) in the cylindrical coordinate ($\boldsymbol{\rho}$, $\boldsymbol{\varphi}$, $\boldsymbol{z}$), and the only non-zero components are Hz, $E\varphi$, and $E\rho$, therefore, it can be obtained that

$$\frac{1}{\rho}\frac{\partial H_z}{\partial \varphi} = j\omega\varepsilon E_\rho \tag{3a}$$

$$\frac{\partial H_z}{\partial \rho} = -j\omega\varepsilon E_\varphi \tag{3b}$$

$$\frac{1}{\rho}\left[\frac{\partial(\rho E_\varphi)}{\partial \rho} - \frac{\partial E_\rho}{\partial \varphi}\right] = -j\omega\mu H_z \tag{3c}$$

After eliminating the two terms E_φ and E_ρ in the above formulas, the expression of H_z is rendered as

$$\rho\frac{\partial}{\partial \rho}\left(\rho\frac{\partial H_z}{\partial \rho}\right) - \frac{\rho^2}{\varepsilon}\frac{\partial \varepsilon}{\partial \rho}\frac{\partial H_z}{\partial \rho} + \frac{\partial}{\partial \rho}\frac{\partial H_z}{\partial \varphi} + \omega^2\mu\varepsilon\rho^2 H_z = 0 \tag{4}$$

To derive the solution of Eq. (4), H_z can be expressed by using the method of separating variables [13,14] as

$$H_z(\rho,\varphi) = V(\rho)\Phi(\varphi) = [AJ_m(k\rho) + BY_m(k\rho)]e^{jm\varphi} \tag{5}$$

where Jm and Ym are Bessel function and Neumann function, respectively, A, B are both constants and $k = \omega(\mu\varepsilon)^{1/2}$ is the wave number of the dielectric, m is regarded as the azimuthal mode number, which could be an integer. After that, Eq. (3b) leads to

$$\mathrm{E}_\varphi(\rho,\varphi) = U(\rho)\Phi(\varphi) = jp\left[AJ_m'(k\rho) + BY_m'(k\rho)\right]e^{j\omega\varphi} \tag{6}$$

where $p=(\mu/\varepsilon)^{1/2}$. For E-polarization, the only difference is that the p is changed to $p=(\varepsilon/\mu)1/2$.

Next, we divide the field into the superposition of two waves propagating in the opposite direction, which can be expressed by two Hankel functions [13,14]. For H-polarization, the converging and diverging cylindrical wave components of the magnetic and electric field have the following forms

$$H_z{}^+ = AH_m^{(2)}(k\rho)e^{jm\varphi} \tag{7}$$

$$E_\varphi{}^+ = jpAH_m^{(2)'}(k\rho)e^{jm\varphi} \tag{8}$$

$$E_\varphi{}^+ = jpAH_m^{(2)'}(k\rho)e^{jm\varphi} \tag{9}$$

$$E_\varphi{}^- = jpBH_m^{(1)'}(k\rho)e^{jm\varphi} \tag{10}$$

The total fields of H_z and E_φ are

$$H_z = H_z{}^+ + H_z{}^- \tag{11}$$

$$E_\varphi = E_\varphi{}^+ + E_\varphi{}^- = jpC_m^{(2)}H_z{}^+ + jpC_m^{(1)}H_z{}^- \tag{12}$$

where

$$C_{ml}^{(1,2)} = H_m^{(1,2)'}(k_l\rho) \Big/ H_m^{(1,2)}(k_l\rho) \tag{13}$$

l indicates a certain layer of dielectric.

Then, derive the propagation of cylindrical waves in the same layer of dielectric, as for diverging cylindrical wave, according to Eq. (7), it can be expressed as

$$H_z{}^+(\rho) = \frac{H_m^{(2)}(k\rho)}{H_m^{(2)}(k\rho_0)}AH_m^{(2)}(k\rho_0)e^{jm\varphi} = \frac{H_m^{(2)}(k\rho)}{H_m^{(2)}(k\rho_0)}H_z{}^+(\rho_0) \tag{14a}$$

In the same way, the form of the convergent wave is

$$H_z^-(\rho)=\frac{H_m^{(1)}(k\rho)}{H_m^{(1)}(k\rho_0)}BH_m^{(1)}(k\rho_0)e^{jm\varphi}=\frac{H_m^{(1)}(k\rho)}{H_m^{(1)}(k\rho_0)}H_z^-(\rho_0) \tag{14b}$$

If a matrix **P** is defined to connect the magnetic field components at different positions in the same layer of dielectric, then Eq. (14a) and Eq. (14b) can be associated by **P** as

$$\begin{pmatrix} H_z^+(\rho) \\ H_z^-(\rho) \end{pmatrix}=\mathbf{P}\begin{pmatrix} H_z^+(\rho_0) \\ H_z^-(\rho_0) \end{pmatrix} \tag{15}$$

where

$$\mathbf{P}=\begin{pmatrix} \frac{H_m^{(2)}(k\rho)}{H_m^{(2)}(k\rho_0)} & 0 \\ 0 & \frac{H_m^{(1)}(k\rho)}{H_m^{(1)}(k\rho_0)} \end{pmatrix} \tag{16}$$

After this, when the cylindrical waves are transmitted to the interface of two dielectrics, the tangential components of the electric and magnetic fields (Hz, $E\varphi$) can be derived from Hz^+ and Hz^- through the matrix D.

$$\begin{pmatrix} H_z \\ E_\varphi \end{pmatrix}=\mathbf{D}\begin{pmatrix} H_z^+ \\ H_z^- \end{pmatrix} \tag{17}$$

where

$$\mathbf{D}=\begin{pmatrix} 1 & 1 \\ jpC_m^{(2)} & jpC_m^{(1)} \end{pmatrix} \tag{18}$$

According to the boundary conditions, it can be known that the interface between the two dielectrics should meet

$$\mathbf{D}_1\begin{pmatrix} H_{z1}^+ \\ H_{z1}^- \end{pmatrix}=\mathbf{D}_2\begin{pmatrix} H_{z2}^+ \\ H_{z2}^- \end{pmatrix} \tag{19}$$

where 1, 2 refers to two different dielectrics. And for E-polarization, replacing j with $-j$. Obviously, the above formula can also be written as

$$\begin{pmatrix} H_{z2}^+ \\ H_{z2}^- \end{pmatrix}=\mathbf{D}_2{}^{-1}\mathbf{D}_1\begin{pmatrix} H_{z1}^+ \\ H_{z1}^- \end{pmatrix}=\mathbf{D}_{21}\begin{pmatrix} H_{z1}^+ \\ H_{z1}^- \end{pmatrix}=\begin{pmatrix} d_{11} & d_{12} \\ d_{21} & d_{22} \end{pmatrix}\begin{pmatrix} H_{z1}^+ \\ H_{z1}^- \end{pmatrix} \tag{20}$$

Similarly, define the matrix

$$\mathbf{D_{12}}=\mathbf{D_1^{-1}D_2}=\begin{pmatrix} d'_{11} & d'_{12} \\ d'_{21} & d'_{22} \end{pmatrix} \tag{21}$$

Now, let a layer of dielectric 1 and a layer of dielectric 2 be a period, then the electromagnetic wave components inside and outside a period can be expressed by the above matrix as

$$\begin{pmatrix} H_{z2}^+(\rho_2) \\ H_{z1}^-(\rho_2) \end{pmatrix}=\mathbf{D}_{12}\mathbf{P}_2\mathbf{D}_{21}\mathbf{P}_1\begin{pmatrix} H_{z2}^+(\rho_0) \\ H_{z1}^-(\rho_0) \end{pmatrix} \tag{22}$$

By extending the period of the dielectric to the internal and external interface of the Nth period, a general conclusion can be obtained as [13].

$$\begin{pmatrix} H_{z2}^+(\rho_{N+1}) \\ H_{z1}^-(\rho_{N+1}) \end{pmatrix}=\mathbf{D}_{12}\mathbf{P}_2\mathbf{D}_{21}\mathbf{P}_1\begin{pmatrix} H_{z2}^+(\rho_N) \\ H_{z1}^-(\rho_N) \end{pmatrix} \tag{23}$$

where

$$d_{11}=-j\varepsilon_2\sqrt{\frac{\varepsilon_0}{\mu_0}}\frac{\pi}{4}K\rho_1H_m^{(2)}(k_2\rho_1)H_m^{(1)}(k_2\rho_1)\left[p_2C_{m2}^{(1)}-p_1C_{m1}^{(1)}\right] \tag{24a}$$

$$d_{12}=-j\varepsilon_2\sqrt{\frac{\varepsilon_0}{\mu_0}}\frac{\pi}{4}K\rho_1H_m^{(2)}(k_2\rho_1)H_m^{(1)}(k_2\rho_1)\left[p_2C_{m2}^{(1)}-p_1C_{m1}^{(1)}\right] \tag{24b}$$

$$d_{21}=-j\varepsilon_2\sqrt{\frac{\varepsilon_0}{\mu_0}}\frac{\pi}{4}K\rho_1H_m^{(2)}(k_2\rho_1)H_m^{(1)}(k_2\rho_1)\left[p_1C_{m1}^{(2)}-p_2C_{m2}^{(2)}\right] \tag{24c}$$

$$d_{22}=-j\varepsilon_2\sqrt{\frac{\varepsilon_0}{\mu_0}}\frac{\pi}{4}K\rho_1H_m^{(2)}(k_2\rho_1)H_m^{(1)}(k_2\rho_1)\left[p_1C_{m1}^{(1)}-p_2C_{m2}^{(2)}\right] \tag{24d}$$

$$d'_{11}=-j\varepsilon_1\sqrt{\frac{\varepsilon_0}{\mu_0}}\frac{\pi}{4}K\rho_2H_m^{(2)}(k_1\rho_2)H_m^{(1)}(k_1\rho_2)\left[p_2C_{m2}^{(1)}-p_1C_{m1}^{(1)}\right] \tag{25a}$$

$$d'_{12}=-j\varepsilon_1\sqrt{\frac{\varepsilon_0}{\mu_0}}\frac{\pi}{4}K\rho_2H_m^{(2)}(k_1\rho_2)H_m^{(1)}(k_1\rho_2)\left[p_2C_{m2}^{(1)}-p_1C_{m1}^{(1)}\right] \tag{25b}$$

$$d'_{21}=-j\varepsilon_1\sqrt{\frac{\varepsilon_0}{\mu_0}}\frac{\pi}{4}K\rho_2H_m^{(2)}(k_1\rho_2)H_m^{(1)}(k_1\rho_2)\left[p_1C_{m1}^{(2)}-p_2C_{m2}^{(2)}\right] \tag{25c}$$

$$d'_{22}=-j\varepsilon_1\sqrt{\frac{\varepsilon_0}{\mu_0}}\frac{\pi}{4}K\rho_2H_m^{(2)}(k_1\rho_2)H_m^{(1)}(k_1\rho_2)\left[p_1C_{m1}^{(1)}-p_2C_{m2}^{(2)}\right] \tag{25d}$$

and $p1=(\mu0/\varepsilon0\varepsilon1)^{1/2}$, $p2=(\mu0/\varepsilon0\varepsilon2)^{1/2}$, $k1=j(k\varphi^2-\omega^2\mu0\varepsilon0\varepsilon1)^{1/2}$, $k2=j(k\varphi^2-\omega^2\mu0\varepsilon0\varepsilon2)^{1/2}$, ε0, μ0 are the dielectric constant and permeability in a vacuum, and $\varepsilon1$, $\varepsilon2$ are the dielectric constants of the two dielectrics, respectively. The refractive index and dielectric constant of the dielectric layers are approximately satisfied $n_i=\varepsilon_i^{1/2}$. When defining $\mathbf{M}=\mathbf{D_{12}P_2D_{21}P_1}$, after further calculation we can get the conclusion that

$$\mathbf{M}=\mathbf{D}_{12}\mathbf{P}_2\mathbf{D}_{21}\mathbf{P}_1=\begin{pmatrix} \frac{H_m^{(2)}(k_2\rho_2)}{H_m^{(2)}(k_2\rho_1)}\frac{H_m^{(2)}(k_1\rho_1)}{H_m^{(2)}(k_1\rho_0)}d'_{11}d_{11}+\frac{H_m^{(1)}(k_2\rho_2)}{H_m^{(1)}(k_2\rho_1)}\frac{H_m^{(2)}(k_1\rho_1)}{H_m^{(2)}(k_1\rho_0)}d'_{12}d_{21} & \frac{H_m^{(2)}(k_2\rho_2)}{H_m^{(2)}(k_2\rho_1)}\frac{H_m^{(1)}(k_1\rho_1)}{H_m^{(1)}(k_1\rho_0)}d'_{11}d_{12}+\frac{H_m^{(1)}(k_2\rho_2)}{H_m^{(1)}(k_2\rho_1)}\frac{H_m^{(1)}(k_1\rho_1)}{H_m^{(1)}(k_1\rho_0)}d'_{12}d_{22} \\ \frac{H_m^{(2)}(k_2\rho_2)}{H_m^{(2)}(k_2\rho_1)}\frac{H_m^{(2)}(k_1\rho_1)}{H_m^{(2)}(k_1\rho_0)}d'_{21}d_{11}+\frac{H_m^{(1)}(k_2\rho_2)}{H_m^{(1)}(k_2\rho_1)}\frac{H_m^{(2)}(k_1\rho_1)}{H_m^{(2)}(k_1\rho_0)}d'_{22}d_{21} & \frac{H_m^{(2)}(k_2\rho_2)}{H_m^{(2)}(k_2\rho_1)}\frac{H_m^{(1)}(k_1\rho_1)}{H_m^{(1)}(k_1\rho_0)}d'_{21}d_{12}+\frac{H_m^{(1)}(k_2\rho_2)}{H_m^{(1)}(k_2\rho_1)}\frac{H_m^{(1)}(k_1\rho_1)}{H_m^{(1)}(k_1\rho_0)}d'_{22}d_{22} \end{pmatrix} \tag{26}$$

and

$$\begin{pmatrix} H_{z1}^+(\rho_{N+1}) \\ H_{z1}^-(\rho_{N+1}) \end{pmatrix}=\mathbf{M}\begin{pmatrix} H_{z1}^+(\rho_N) \\ H_{z1}^-(\rho_N) \end{pmatrix} \tag{27}$$

In addition, according to Bloch's principle, when the initial radius ρ_0 is relatively large, the transmission of cylindrical waves approximately satisfies the relationship that

$$\begin{pmatrix} H_{z1}^+(\rho_{N+1}) \\ H_{z1}^-(\rho_{N+1}) \end{pmatrix}=e^{jkd}\begin{pmatrix} H_{z1}^+(\rho_N) \\ H_{z1}^-(\rho_N) \end{pmatrix} \tag{28}$$

Combining Eqs. (27) and (28) and gradually simplifying them yields the following result(see Appendix for detailed calculation procedure):

$$e^{jkd}+e^{-jkd}=\frac{H_m^{(2)}(k_2\rho_2)}{H_m^{(2)}(k_2\rho_1)}\frac{H_m^{(2)}(k_1\rho_1)}{H_m^{(2)}(k_1\rho_0)}d_{11}'d_{11}+\frac{H_m^{(1)}(k_2\rho_2)}{H_m^{(1)}(k_2\rho_1)}\frac{H_m^{(2)}(k_1\rho_1)}{H_m^{(2)}(k_1\rho_0)}d_{12}'d_{21}+\frac{H_m^{(2)}(k_2\rho_2)}{H_m^{(2)}(k_2\rho_1)}\frac{H_m^{(1)}(k_1\rho_1)}{H_m^{(1)}(k_1\rho_0)}d_{21}'d_{12}+\frac{H_m^{(1)}(k_2\rho_2)}{H_m^{(1)}(k_2\rho_1)}\frac{H_m^{(1)}(k_1\rho_1)}{H_m^{(1)}(k_1\rho_0)}d_{22}'d_{22} \tag{29}$$

Obviously, the left side of Eq. (29) equals a typical Eulerian formula and the right side is equal to the trace of the matrix **M**, i.e.

$$\cos kd=\frac{\mathbf{M}(1,1)+\mathbf{M}(2,2)}{2} \tag{30}$$

Obviously, this conclusion is very consistent in form with that drawn in 1D PCs.

Now, we take the graphene layer as the main defect layer and derive the conditions for it to excite OTS. Regarding the conductivity of graphene, a clear calculation method has been given by the Kubo formula as [26].

$$\sigma_g=\sigma_g^{\text{inter}}+\sigma_g^{\text{intra}} \tag{31}$$

where the superscripts "inter" and "intra" indicate the conductivity interband and intraband, respectively, which can be written as

$$\sigma_g^{\text{intra}}=\frac{je^2k_BT}{\pi\hbar^2(\omega+j/\tau)}\left(\frac{\mu_C}{k_BT}+2\ln\left(e^{-\frac{\mu_C}{k_BT}}+1\right)\right) \tag{32}$$

$$\sigma_g^{\text{inter}}=j\frac{e^2}{4\pi\hbar}\ln\left|\frac{2\mu_C-\hbar(\omega+j/\tau)}{2\mu_C+\hbar(\omega+j/\tau)}\right| \tag{33}$$

where e is the electron charge, k_B is the Boltzmann constant, T is the thermodynamic temperature, ω is the angular frequency of the cylindrical wave, τ is the phenomenological scattering rate, and μ_C is the chemical potential of the graphene, respectively.

The effective permittivity of graphene has the form that [29].

$$\varepsilon_g=1+j\sigma_g/\omega\varepsilon_0 d_G \tag{34}$$

when assuming that the external factors do not affect the electronic band structure of the graphene layer at all, where ε_0 is the permittivity of vacuum and d_G is defined as the thickness of graphene.

With the above conclusions, the propagation characteristics of cylindrical waves in the graphene layer can be drawn. Firstly, assume that $\rho_{-1}=\rho_0-d_G$ is the radius of the inner boundary of graphene, and ρ_0 is the outside one. From Eq. (18), the matrix of the graphene layer can be written as

$$\mathbf{D_{Ga}}=\begin{pmatrix}1 & 1\\ jp_GC_m^{(2)}(k_{G\rho}\rho_a) & jp_GC_m^{(1)}(k_{G\rho}\rho_a)\end{pmatrix},\ (a=0,1) \tag{35}$$

and

$$\mathbf{P_G}=\begin{pmatrix}\frac{H_m^{(2)}(k_{G\rho}\rho_0)}{H_m^{(2)}(k_{G\rho}\rho_{-1})} & 0\\ 0 & \frac{H_m^{(1)}(k_{G\rho}\rho_0)}{H_m^{(1)}(k_{G\rho}\rho_{-1})}\end{pmatrix} \tag{36}$$

For the air layer at $\rho=\rho_{-1}$, there is

$$\mathbf{D_0}=\begin{pmatrix}1 & 1\\ jp_0C_m^{(2)}(k_{0\rho}\rho_{-1}) & jp_0C_m^{(1)}(k_{0\rho}\rho_{-1})\end{pmatrix} \tag{37}$$

where the subscripts G and 0 represent the graphene layer and air, respectively, while the subscripts ρ represents the component of the wave vector k in the ρ-direction. Therefore, at the interface between the two adjacent media with the defect layer, the magnetic field components can be connected by the matrix $\mathbf{D_G}$, $\mathbf{P_G}$, and $\mathbf{D_0}$ as

$$\begin{pmatrix}H_{z0}^{+}(\rho_{-1})\\ H_{z0}^{-}(\rho_{-1})\end{pmatrix}=\mathbf{D_0}^{-1}\mathbf{D_G}\begin{pmatrix}H_{zG}^{+}(\rho_{-1})\\ H_{zG}^{-}(\rho_{-1})\end{pmatrix}=\mathbf{D_0}^{-1}\mathbf{D_{G-1}}\mathbf{P_G}^{-1}\mathbf{D_{G0}}^{-1}\begin{pmatrix}H_z(\rho_0)\\ E_\varphi(\rho_0)\end{pmatrix}=\mathbf{T}\begin{pmatrix}H_z(\rho_0)\\ E_\varphi(\rho_0)\end{pmatrix} \tag{38}$$

In addition, it is easy to be calculated by Eqs. (27) and (28) that

$$\mathbf{X}=\begin{pmatrix}1\\ \frac{e^{jkd}-\mathbf{M}(1,1)}{\mathbf{M}(1,2)}\end{pmatrix} \tag{39}$$

is one of the eigenvectors of the two equations. To excite OTS [24], the electromagnetic wave needs to be evanescent in the ρ-direction, so the wave vector k in the ρ-direction in the air should be imaginary, namely $k_{0\rho}=j[k_\varphi^2-(\omega/c)^2]^{1/2}$ and it needs to be attenuated in the ρ-direction, so, the magnetic field in the air inside the defect layer can only be in the following form

$$H(\rho,\varphi)=H_{\rho<\rho_{-1}}^{-}e^{\left(\int jk_\varphi\rho d\varphi-ik_{0\rho}\rho\right)} \tag{40}$$

the component $H_{0\rho}^{+}$ along the ρ^+ direction is equal to 0. Substituting Eq. (39), Eq. (40) into Eq. (38), the condition for exciting the OTS is to satisfy

$$\mathbf{T}(1,1)+\mathbf{T}(1,2)\mathbf{X}(2)=0 \tag{41}$$

In addition to the above formula, it also needs to meet that the imaginary part of k is above 0, and the dispersion curve is below $\omega/k_0=c$.

The difference between the H- and E-polarization is only in the form of some elements in the matrix **P** and **D**, and the other calculation processes are completely the same.

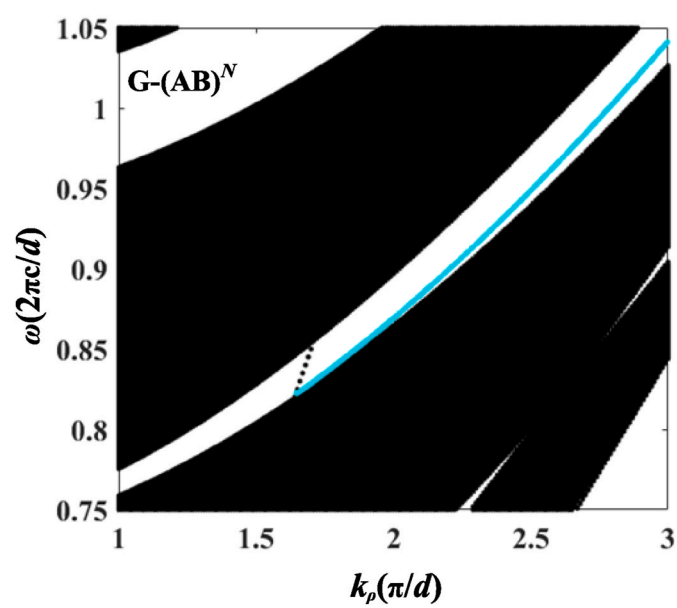

Fig. 2. Dispersion curve of excited OTS under G-(AB)N structure. The white and black regions represent the forbidden and passbands of the periodic structure, respectively, while the black dashed line fulfills the equation ω/k0 = c. When the OTS is excited, the light blue solid line corresponds to the relationship between the angular frequency ω of the input electromagnetic wave and the ρ-directional component of the wave vector k. (For interpretation of the references to color in this figure legend, the reader is referred to the Web version of this article.)

3. Analysis and discussion

As shown in Fig. 1, the initial parameters are: $d = 30.5$ μm, $d_A = 0.24d$, $d_B = 0.76d$, $d_G = 1.1148 \times 10^{-5}d$, $\rho_{-1} = 0.1d$, the azimuthal mode number $m = 0$. The refractive index of A and B are described by n_A and n_B, which are 2.96 and 1.778. $T = 300$ K, the chemical potential μ_C of graphene equals 0.3 eV, phenomenological scattering rate $\tau = 10^{-13}$ s [31]. The thickness d_0 of the C layer is set to be 50 times the wavelength of the incident light in a vacuum λ_0 and the refractive index $n_0 = 1$. In this paper, this structure is denoted as G-(AB)^N. Since the excitation of the Tamm state is independent of the period number N of the structure, for convenience, N is fixed to 10. The dispersion curve obtained according to the formula derived above is exhibited in Fig. 2. Where the black part is the passband of the periodic structure, while the white part represents the forbidden band, and the black dotted line satisfies equation $\omega/k_0 = c$, the dispersion curve needs to be below it. The light blue curve in Fig. 2 is the corresponding relationship between the ρ-direction component of the wave vector k in the cylindrical coordinate system and the angular frequency ω of the incident electromagnetic wave when the OTS is excited.

Comparing the passband distribution of the 1D planar PCs with the same parameters, it is not difficult to find in Fig. 2 that when the initial radius ρ_0 is large enough, the dispersion of the CPCs is basically the same as that under the 1D condition, which can also, to a certain degree, prove the correctness of the formula derivation in the second part. Obviously, there is a positive correlation between k_z and ω.

Next, as illustrated in Fig. 3(a)-(c), substitute GABG, GAG, GAGAG for the G layer in Fig. 1, keeping the initial radius $\rho_{-1} = 0.1d$ and all other parameters unchanged. Since the periodic parts of the four structures are thoroughly identical, i.e., they have the same passband and forbidden band distributions, which means that we can represent the resultant curves of the four structures in a single Fig. 3(d). From Fig. 3(d), it can be observed that the trends of the dispersion curves are very similar for both G-(AB)^N and GABG-(AB)^N structures, but when k_ρ is the same, the ω corresponding to the excitation OTS of the GABG-(AB)^N structure is generally larger than that of G-(AB)^N by 0.0039 ($2\pi c/d$) on average. With k_ρ between 1.714 (π/d) and 2.267 (π/d), the GAGAG-(AB)^N excitation OTS has the largest ω of the four structures, while the GAG-(AB)^N structure has a higher value when k increase to 2.267 (π/d). The curve of GAGAG-(AB)^N intersects GAG-(AB)^N and GABG-(AB)^N at 0.9362 ($2\pi c/d$) and 1.0338 ($2\pi c/d$) for k_ρ equal to 2.267 (π/d) and 2.940 (π/d), respectively.

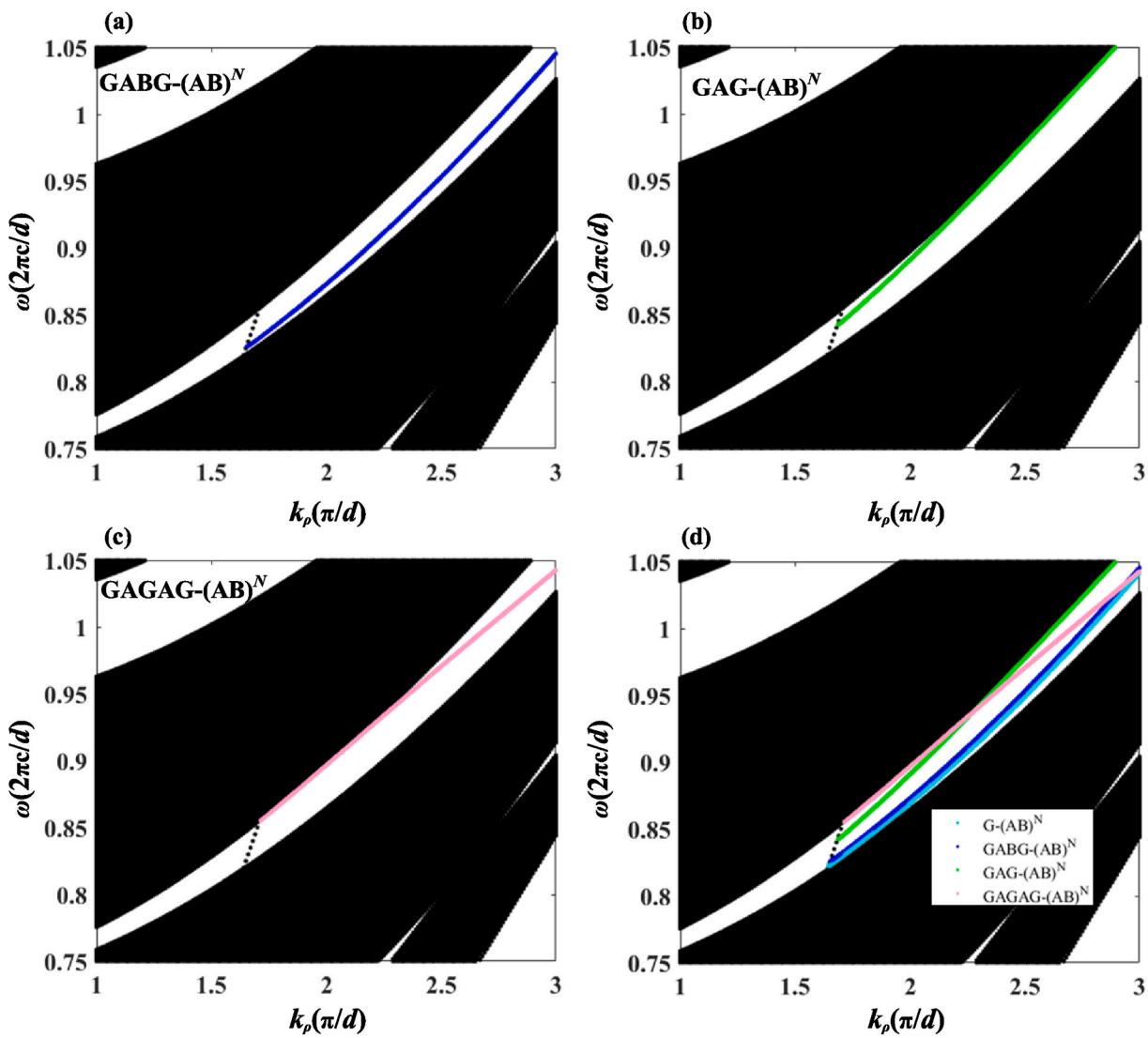

Fig. 3. Dispersion curves of excited OTS under different structures: (a) GABG-(AB)N, (b) GAG-(AB)N, (c) GAGAG-(AB)N, and (d) all the curves. The white and black regions represent the forbidden and passbands of the periodic structure, respectively, while the black dashed line fulfills the equation ω/k0 = c. The colored curves in all figures represent the relationship between the angular frequency ω of the input electromagnetic wave and the ρ-directional component of the wave vector k under the respective structures when the OTS is excited.

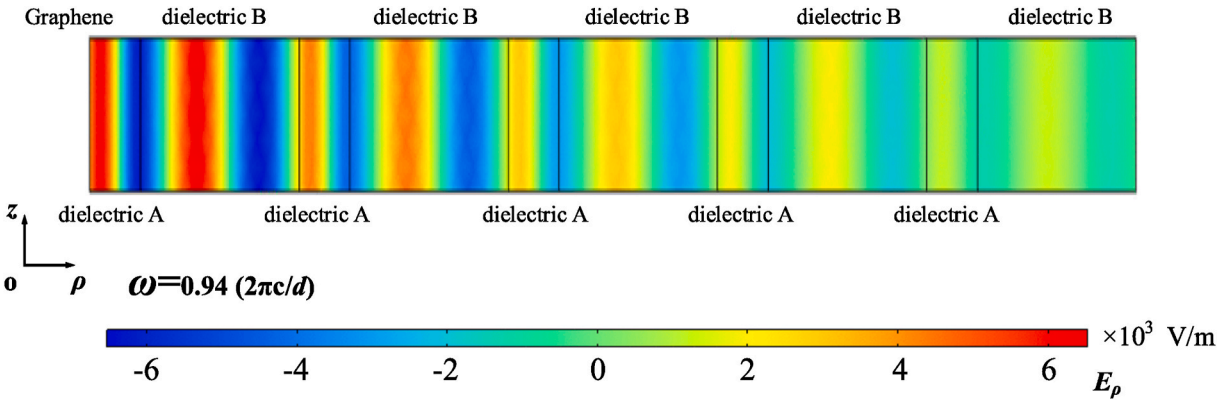

Fig. 4. Distribution of electric field intensity in ρ-direction in G-(AB)N structure when ω = 0.94 (2πc/d).

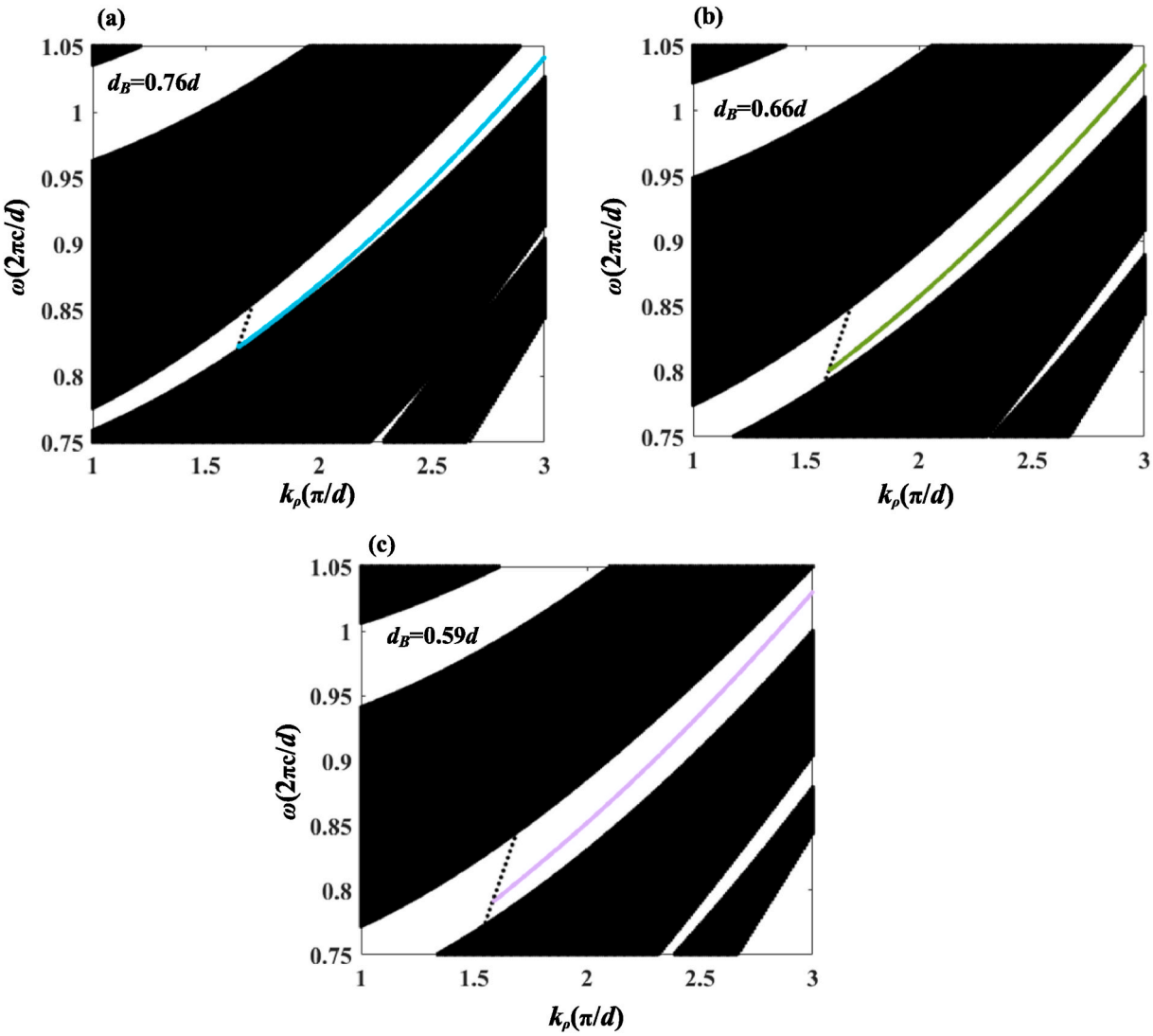

Fig. 5. Dispersion curve of excited OTS under the G-(AB)N structure with different thickness of dielectric B: (a) dB = 0.76d, (b) dB = 0.66d and (c) dB = 0.59d. The white and black regions represent the forbidden and passbands of the periodic structure, respectively, while the black dashed line fulfills the equation ω/k0 = c. The colored curves in all figures represent the relationship between the angular frequency ω of the input electromagnetic wave and the ρ-directional component of the wave vector k under the respective structures when the OTS is excited.

Fig. 4 reveals the distribution of the electric field intensity in the ρ-direction of an electromagnetic wave incident at an angular frequency $\omega = 0.94\ (2\pi c/d)$ in the G-(AB)^N structure. Since the refractive index of dielectric C n_0 equals 1, whose thickness is much larger than other dielectrics and is an integer multiple of the wavelength of the incident wave in a vacuum, according to the principle of TMM, adding or deleting

the C layer has no effect on the distribution of electric field, therefore, layer C is omitted in Fig. 4 for a more visual representation. Moreover, rectangles are used here to replace the cross-section of the CPCs with a large radius. Because the thickness of graphene is four orders of magnitude smaller than the other two dielectrics, it is not easy to observe the graphene layer in Fig. 4 directly. But it is easy to conclude that the introduction of defects makes the electric field tend to be confined to the surface, and the attenuation to the side of the periodic structure is greater, which also provides evidence for the defect layer to excite OTS.

In addition to adopting diverse defect layer structures, different curves can also be obtained by changing the thickness of the general dielectric. Keep other conditions unchanged, in the most basic G-(AB)^N structure, the thickness of the dielectric B (d_B) are severally taken as 0.76d, 0.66d, and 0.59d, and the resulting image is shown in Fig. 5. On the one hand, the change in the thickness of dielectric B, at the same time, alters the periodic structure that causes the disparity in the distribution of the passband and the forbidden band. As d_B decreases, the forbidden band of the dispersion curve in Fig. 5 becomes wider. When we take $k_\rho = 2(\pi/d)$, the three different dB values correspond to the passband widths of 0.0322 (2πc/d) (0.8646 (2πc/d)-0.8968 (2πc/d)), 0.0479 (2πc/d) (0.8441 (2πc/d)-0.8920 (2πc/d)) and 0.0557 (2πc/d) (0.8309 (2πc/d)-0.8866 (2πc/d)) respectively. But on the other hand, the dispersion curves themselves have very slight disparities both in trend and in value as indicated in the several graphs in Fig. 5. At $k_\rho = 2(\pi/d)$, d_B takes 0.76d, 0.66d, and 0.59d corresponding to ω as 0.8691 (2πc/d), 0.8571 (2πc/d) and 0.8520 (2πc/d).

Now, we use GABG as the defect layer, and its structure will change as d_B takes different values. Same as Fig. 5, set d_B to 0.76d, 0.66d, and 0.59d, respectively, and the result is revealed in Fig. 6. At $k_\rho = 2(\pi/d)$, d_B takes 0.76d, 0.66d, and 0.59d corresponding to ω as 0.8730 (2πc/d), 0.8633 (2πc/d) and 0.8588 (2πc/d).

Evidently, in Figs. 5 and 6, the same d_B demonstrates the same passband and forbidden band distribution, while in Fig. 6, even if the structure of the defective layer is changed while adjusting the dielectric thickness, the difference in the values between the three curves (when $k_\rho = 2(\pi/d)$, d_B takes the value from 0.76d to 0.59d, ω changes 0.0142 (2πc/d)) is still very similar or even smaller than that shown in Fig. 5 (ω is changed 0.0171 (2πc/d)).

Besides, the phenomenological scattering rate τ and chemical

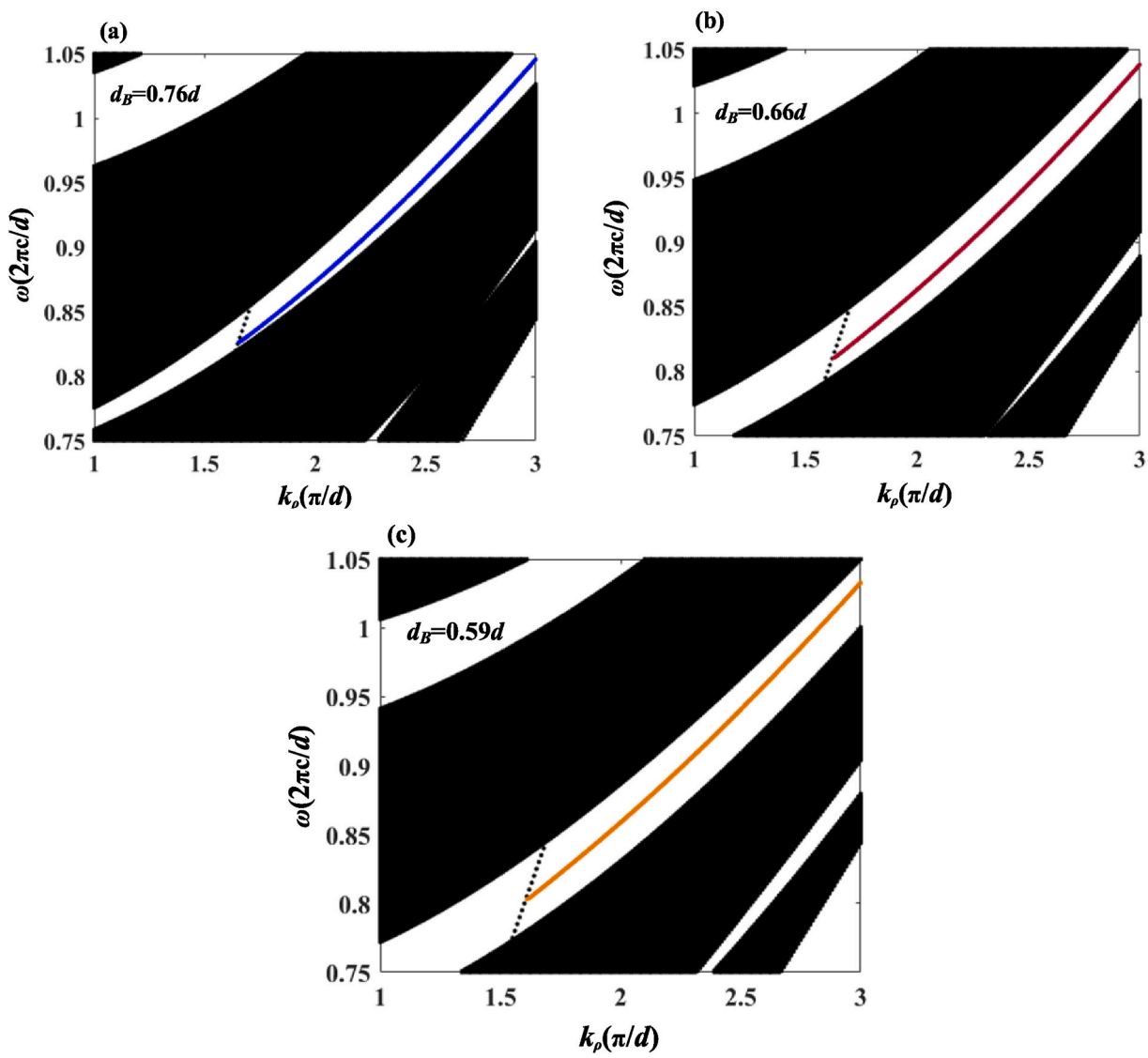

Fig. 6. The dispersion curves of excited OTS under the GABG-(AB)N structure with different thicknesses of dielectric B:(a) dB = 0.76d, (b) dB = 0.66d, and (c) dB = 0.59d. The white and black regions represent the forbidden and passbands of the periodic structure, respectively, while the black dashed line fulfills the equation ω/k0 = c. The colored curves in all figures represent the relationship between the angular frequency ω of the input electromagnetic wave and the ρ-directional component of the wave vector k under the respective structures when the OTS is excited.

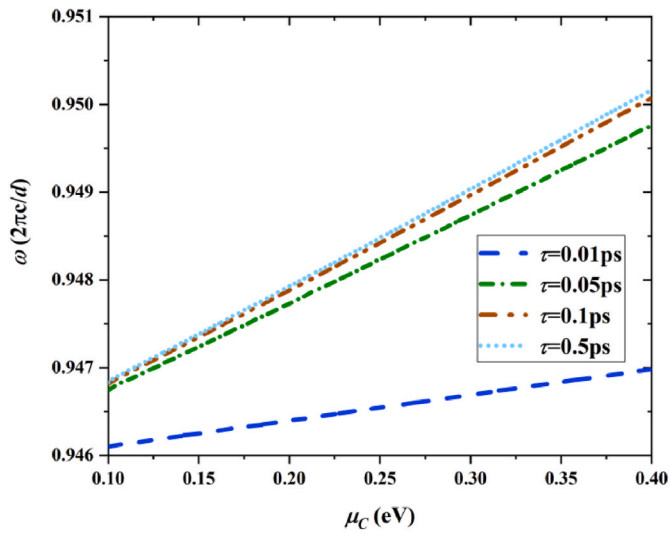

Fig. 7. Chemical potential and phenomenological scattering rate dependence of dispersion relations when kz = 2.5(π/d).

potential μ_C of graphene will also influence the dispersion curve.

The data in Fig. 7 displays the angular frequency ω of the incident cylindrical wave required to excite OTS when the chemical potential μ_C transmutes from 0.1 eV to 0.4 eV, where k_z takes 2.5 (π/d), the phenomenological scattering rate τ are independently set to 0.01 ps, 0.05 ps, 0.1 ps, and 0.5 ps In general, the increase in chemical potential and phenomenological scattering rate will make the same k_z correspond to a larger ω. Among them, the change caused by the chemical potential is closer to a linear relationship. However, as the phenomenological scattering rate increases, the numerical change gradually becomes insignificant, especially when $\tau > 0.5$ ps, the difference in ω is so trifling that these curves almost coincide. It can be concluded that by adjusting the data of μ_C and τ, the electromagnetic waves of various angular frequencies can excite OTS, and a smaller phenomenological scattering rate means higher accuracy (the slope of the curve is smaller, and when $\tau = 0.01$ ps, modulation range is 0.0008715 (2πc/d) (0.9461045 (2πc/d)-0.9469760 (2πc/d))), while if a larger modulation range is required, choose a larger τ (when $\tau = 0.1$ ps, modulation range is 0.003177 (2πc/d) (0.9468210 (2πc/d)-0.9499980 (2πc/d))).

4. Conclusion

In summary, we have further derived the conditions for excitation of OTS in the CPCs based on the existing theory, and both E-polarization and H-polarization are investigated. After that, we established CPCs with graphene as the main doped defect layer and periodic structures, which verify the correctness of the formula. The electric field intensity distribution in the structure can also indicate the existence of OTS. On this point, altering the structure of the defect layer will cause the dispersion curve to show distinct trends. The selection of different thicknesses of the dielectric layer affects the position of the passband and the forbidden band, but the dispersion curve itself moves slightly. The chemical potential of graphene dependence of the k_ρ-ω curve is more likely to be a kind of positive correlation. While phenomenological scattering rate has the weakest effect on the results. In general, the effect of these changes on the final results of the dispersion curves is relatively small, but it does allow for finer modulation of specific wave vectors and angular frequencies, which provides ideas and a theoretical basis for the design of sensors and other devices.

Credit author statement

Jia-Tao Zhang, and Hai-Feng Zhang contributed to the novel idea of the study; Si–Si Rao and Dan Zhang contributed significantly to analysis and manuscript preparation; Hai-Feng Zhang performed the data analyses and wrote the manuscript.

Declaration of competing interest

The authors declare that they have no known competing financial interests or personal relationships that could have appeared to influence the work reported in this paper.

Acknowledgement

This work was supported by the College Student Innovation Training Program of Nanjing University of Posts and Telecommunications, and the Jiangsu Agriculture Science and Technology Innovation Fund (JASTIF) (Grant No.CX(21)3187).

Appendix

$$\begin{aligned}
\det\left(\mathbf{M}-e^{jkd}\right) = {} & \left[\frac{H_m^{(2)}(k_2\rho_2)}{H_m^{(2)}(k_2\rho_1)}\right]^2 \frac{H_m^{(2)}(k_1\rho_1)}{H_m^{(2)}(k_1\rho_0)}\frac{H_m^{(1)}(k_1\rho_1)}{H_m^{(1)}(k_1\rho_0)} d'_{11}d'_{21}d_{11}d_{12} + \frac{H_m^{(2)}(k_2\rho_2)}{H_m^{(2)}(k_2\rho_1)}\frac{H_m^{(2)}(k_1\rho_1)}{H_m^{(2)}(k_1\rho_0)}\frac{H_m^{(1)}(k_2\rho_2)}{H_m^{(1)}(k_2\rho_1)}\frac{H_m^{(1)}(k_1\rho_1)}{H_m^{(1)}(k_1\rho_0)} d'_{11}d'_{22}d_{11}d_{22} \\
& + \frac{H_m^{(1)}(k_2\rho_2)}{H_m^{(1)}(k_2\rho_1)}\frac{H_m^{(2)}(k_1\rho_1)}{H_m^{(2)}(k_1\rho_0)}\frac{H_m^{(2)}(k_2\rho_2)}{H_m^{(2)}(k_2\rho_1)}\frac{H_m^{(1)}(k_1\rho_1)}{H_m^{(1)}(k_1\rho_0)} d'_{12}d'_{21}d_{12}d_{21} + \left[\frac{H_m^{(1)}(k_2\rho_2)}{H_m^{(1)}(k_2\rho_1)}\right]^2 \frac{H_m^{(2)}(k_1\rho_1)}{H_m^{(2)}(k_1\rho_0)}\frac{H_m^{(1)}(k_1\rho_1)}{H_m^{(1)}(k_1\rho_0)} d'_{12}d'_{22}d_{21}d_{22} - \left[\frac{H_m^{(2)}(k_2\rho_2)}{H_m^{(2)}(k_2\rho_1)}\frac{H_m^{(2)}(k_1\rho_1)}{H_m^{(2)}(k_1\rho_0)} d'_{11}d_{11}\right. \\
& \left. + \frac{H_m^{(1)}(k_2\rho_2)}{H_m^{(1)}(k_2\rho_1)}\frac{H_m^{(2)}(k_1\rho_1)}{H_m^{(2)}(k_1\rho_0)} d'_{12}d_{21} + \frac{H_m^{(2)}(k_2\rho_2)}{H_m^{(2)}(k_2\rho_1)}\frac{H_m^{(1)}(k_1\rho_1)}{H_m^{(1)}(k_1\rho_0)} d'_{21}d_{12} + \frac{H_m^{(1)}(k_2\rho_2)}{H_m^{(1)}(k_2\rho_1)}\frac{H_m^{(1)}(k_1\rho_1)}{H_m^{(1)}(k_1\rho_0)} d'_{22}d_{22} - e^{jkd}\right] e^{jkd} - \left\{\left[\frac{H_m^{(2)}(k_2\rho_2)}{H_m^{(2)}(k_2\rho_1)}\right]^2 \frac{H_m^{(1)}(k_1\rho_1)}{H_m^{(1)}(k_1\rho_0)}\frac{H_m^{(2)}(k_1\rho_1)}{H_m^{(2)}(k_1\rho_0)} d'_{11}d'_{21}d_{11}d_{12}\right. \\
& + \frac{H_m^{(2)}(k_2\rho_2)}{H_m^{(2)}(k_2\rho_1)}\frac{H_m^{(1)}(k_1\rho_1)}{H_m^{(1)}(k_1\rho_0)}\frac{H_m^{(1)}(k_2\rho_2)}{H_m^{(1)}(k_2\rho_1)}\frac{H_m^{(2)}(k_1\rho_1)}{H_m^{(2)}(k_1\rho_0)} d'_{11}d'_{22}d_{12}d_{21} + \frac{H_m^{(1)}(k_2\rho_2)}{H_m^{(1)}(k_2\rho_1)}\frac{H_m^{(1)}(k_1\rho_1)}{H_m^{(1)}(k_1\rho_0)}\frac{H_m^{(2)}(k_2\rho_2)}{H_m^{(2)}(k_2\rho_1)}\frac{H_m^{(2)}(k_1\rho_1)}{H_m^{(2)}(k_1\rho_0)} d'_{12}d'_{21}d_{11}d_{22} \\
& \left. + \left[\frac{H_m^{(1)}(k_2\rho_2)}{H_m^{(1)}(k_2\rho_1)}\right]^2 \frac{H_m^{(1)}(k_1\rho_1)}{H_m^{(1)}(k_1\rho_0)}\frac{H_m^{(2)}(k_1\rho_1)}{H_m^{(2)}(k_1\rho_0)} d'_{12}d'_{22}d_{21}d_{22}\right\} \\
& = 0
\end{aligned} \tag{42}$$

Eq. (42) can be reduced to the following form

$$\frac{H_m^{(2)}(k_2\rho_2)}{H_m^{(2)}(k_2\rho_1)}\frac{H_m^{(2)}(k_1\rho_1)}{H_m^{(2)}(k_1\rho_0)}d_{11}^{'}d_{11}+\frac{H_m^{(1)}(k_2\rho_2)}{H_m^{(1)}(k_2\rho_1)}\frac{H_m^{(2)}(k_1\rho_1)}{H_m^{(2)}(k_1\rho_0)}d_{12}^{'}d_{21}+\frac{H_m^{(2)}(k_2\rho_2)}{H_m^{(2)}(k_2\rho_1)}\frac{H_m^{(1)}(k_1\rho_1)}{H_m^{(1)}(k_1\rho_0)}d_{21}^{'}d_{12}+\frac{H_m^{(1)}(k_2\rho_2)}{H_m^{(1)}(k_2\rho_1)}\frac{H_m^{(1)}(k_1\rho_1)}{H_m^{(1)}(k_1\rho_0)}d_{22}^{'}d_{22}$$
$$=\frac{H_m^{(2)}(k_2\rho_2)}{H_m^{(2)}(k_2\rho_1)}\frac{H_m^{(2)}(k_1\rho_1)}{H_m^{(2)}(k_1\rho_0)}\frac{H_m^{(1)}(k_2\rho_2)}{H_m^{(1)}(k_2\rho_1)}\frac{H_m^{(1)}(k_1\rho_1)}{H_m^{(1)}(k_1\rho_0)}\left[(d_{11}d_{22}-d_{12}d_{21})\left(d_{11}^{'}d_{22}^{'}-d_{12}^{'}d_{21}^{'}\right)\right]e^{-jkd}+e^{jkd} \tag{43}$$

noticed that

$$(d_{11}d_{22}-d_{12}d_{21})\left(d_{11}^{'}d_{22}^{'}-d_{12}^{'}d_{21}^{'}\right)=\varepsilon_1^2\varepsilon_2^2\frac{\varepsilon_0^2}{\mu_0^2}\frac{\pi^4}{256}K^4\rho_1^2\rho_2^2\left[H_m^{(2)}(k_2\rho_1)H_m^{(1)}(k_2\rho_1)H_m^{(2)}(k_1\rho_2)H_m^{(1)}(k_1\rho_2)\right]^2\cdot$$
$$p_1^2p_2^2\left[C_m^{(1)}(k_1\rho_1)-C_m^{(2)}(k_1\rho_1)\right]\left[C_m^{(1)}(k_2\rho_1)-C_m^{(2)}(k_2\rho_1)\right]\left[C_m^{(1)}(k_1\rho_2)-C_m^{(2)}(k_1\rho_2)\right]\left[C_m^{(1)}(k_2\rho_2)-C_m^{(2)}(k_2\rho_2)\right] \tag{44}$$

where

$$\left[C_m^{(1)}(k_1\rho_1)-C_m^{(2)}(k_1\rho_1)\right]\left[C_m^{(1)}(k_2\rho_1)-C_m^{(2)}(k_2\rho_1)\right]=-\frac{1}{H_m^{(1)}(k_1\rho_1)H_m^{(2)}(k_1\rho_1)H_m^{(1)}(k_2\rho_1)H_m^{(2)}(k_2\rho_1)}\frac{16}{\pi^2}\frac{1}{k_1k_2\rho_1^2} \tag{45}$$

$$\left[C_m^{(1)}(k_1\rho_2)-C_m^{(2)}(k_1\rho_2)\right]\left[C_m^{(1)}(k_2\rho_2)-C_m^{(2)}(k_2\rho_2)\right]=-\frac{1}{H_m^{(1)}(k_1\rho_2)H_m^{(2)}(k_1\rho_2)H_m^{(1)}(k_2\rho_2)H_m^{(2)}(k_2\rho_2)}\frac{16}{\pi^2}\frac{1}{k_1k_2\rho_2^2} \tag{46}$$

$$\varepsilon_1^2\varepsilon_2^2\frac{\varepsilon_0^2}{\mu_0^2}\frac{\pi^4}{256}K^4\rho_1^2\rho_2^2p_1^2p_2^2\left(\frac{16}{\pi^2}\frac{1}{k_1k_2\rho_1^2}\right)\left(\frac{16}{\pi^2}\frac{1}{k_1k_2\rho_2^2}\right)=1 \tag{47}$$

$$\frac{H_m^{(2)}(k_2\rho_2)}{H_m^{(2)}(k_2\rho_1)}\frac{H_m^{(2)}(k_1\rho_1)}{H_m^{(2)}(k_1\rho_0)}\frac{H_m^{(1)}(k_2\rho_2)}{H_m^{(1)}(k_2\rho_1)}\frac{H_m^{(1)}(k_1\rho_1)}{H_m^{(1)}(k_1\rho_0)}\left[H_m^{(2)}(k_2\rho_1)H_m^{(1)}(k_2\rho_1)H_m^{(2)}(k_1\rho_2)H_m^{(1)}(k_1\rho_2)\right]^2\cdot$$
$$\frac{1}{H_m^{(1)}(k_1\rho_1)H_m^{(2)}(k_1\rho_1)H_m^{(1)}(k_2\rho_1)H_m^{(2)}(k_2\rho_1)}\frac{1}{H_m^{(1)}(k_1\rho_2)H_m^{(2)}(k_1\rho_2)H_m^{(1)}(k_2\rho_2)H_m^{(2)}(k_2\rho_2)}=\frac{H_m^{(1)}(k_1\rho_2)H_m^{(2)}(k_1\rho_2)}{H_m^{(1)}(k_1\rho_0)H_m^{(2)}(k_1\rho_0)} \tag{48}$$

Because the initial radius is large enough, the values of the first and second types of Hankel functions are approximately equal in theory for the corresponding positions in the adjacent periods (when $\rho=\rho_0$ or $\rho=\rho_2$), that means

$$\frac{H_m^{(1)}(k_1\rho_2)H_m^{(2)}(k_1\rho_2)}{H_m^{(1)}(k_1\rho_0)H_m^{(2)}(k_1\rho_0)}=1 \tag{49}$$

Eq. (29) can be obtained from the above calculation.

References

[1] E. Yablonovitch, Inhibited spontaneous emission in solid-state physics and electronics, Phys. Rev. Lett. 58 (20) (1987) 2059.
[2] S. John, Strong localization of photons in certain disordered dielectric super lattices, Phys. Rev. Lett. 58 (23) (1987) 2486–2489.
[3] T.P. Vo, M. Mivelle, Ségolène Callard, A. Rahmani, T. Grosjean, Near-field probing of slow Bloch modes on photonic crystals with a nanoantenna, Opt Express 20 (4) (2012) 4124–4135.
[4] P.E. Barclay, K. Srinivasan, O. Painter, Nonlinear response of silicon photonic crystal microresonators excited via an integrated waveguide and fiber taper, Opt Express 13 (3) (2005).
[5] Y. Akahane, T. Asano, B.S. Song, S. Noda, High-Q photonic nanocavity in a two-dimensional photonic crystal, Nature 425 (6961) (2003) 944–947.
[6] J.C. Knight, T.A. Birks, P.S. Russell, D.M. Atkin, All-silica single-mode optical fiber with photonic crystal cladding, Opt Lett. 21 (19) (1996) 1547–1549.
[7] A. Blanco, E. Chomski, S. Grabtchak, M. Ibisate, S. John, S.W. Leonard, C. Lopez, F. Meseguer, H. Miguez, J.P. Mondia, G.A. Ozin, O. Toader, H.M. van Driel, Large-scale synthesis of a silicon photonic crystal with a complete three-dimensional bandgap near 1.5 micrometres, Nature 405 (2000) 437–440.
[8] Z.Y. Li, L.L. Lin, Photonic band structures solved by a plane-wave-based transfer-matrix method, Phys. Rev. 67 (4 Pt 2) (2003), 046607.
[9] H.M. Peng, B.F. Wan, P.X. Wang, D. Zhang, H.F. Zhang, Tunable omnidirectional band gap properties of 1D plasma annular periodic multilayer structure based on an improved Fibonacci topological structure, Opt. Quant. Electron. 53 (5) (2021) 1–15.
[10] Y.O. Averkov, Y.V. Prokopenko, V.M. Yakovenko, Waves of a magnetoplasma solid-state cylinder under quasi-stationary conditions, IEEE Trans. Plasma Sci. 49 (10) (2021) 3078–3085.
[11] J. Yuan, Y.Y. Lu, X. Antoine, Modeling photonic crystals by boundary integral equations and dirichlet-to-neumann maps, J. Comput. Phys. 227 (9) (2008) 4617–4629.
[12] M.S. Chen, C.J. Wu, T.J. Yang, Optical properties of a superconducting annular periodic multilayer structure, Solid State Commun. 149 (43–44) (2009) 1888–1893.
[13] C.A. Hu, C.J. Wu, T.J. Yang, S.L. Yang, Analysis of optical properties in cylindrical dielectric photonic crystal, Opt Commun. 291 (2013) 424–434.
[14] V.V. Nikolaev, G.S. Sokolovskii, M.A. Kaliteevskii, Bragg reflectors for cylindrical waves, Semiconductors 33 (1999) 147–152.
[15] Y. Jiang, J. Hacker, Cylindrical-wave reflection and antireflection at media interfaces, Appl. Optic 33 (1994) 7431–7434.
[16] T.W. Chang, H.T. Hsu, C.J. Wu, Investigation of photonic band gap in a circular photonic crystal, J. Electromagn. Waves Appl. 25 (16) (2011) 2222–2235.
[17] Y.T. Xiang, B.F. Wan, H.F. Zhang, Multiscale and multiple physical quantities sensor based on nonreciprocal evanescent wave in the one-dimensional photonic crystals, IEEE Sensor. J. 21 (18) (2021) 19984–19992.
[18] Y. Kozawa, S. Sato, T. Sato, Y. Inoue, Y. Ohtera, S. Kawakami, Cylindrical vector laser beam generated by the use of a photonic crystal mirror, APEX 1 (2) (2008) 361–364.
[19] Q. Liu, Comb filtering properties of total reflection tunnelling in cylindrical photonic crystals, Chin. J. Comput. Phys. 29 (1) (2012) 133–138.
[20] El-Naggar, A. Sahar, Photonic gaps in one dimensional cylindrical photonic crystal that incorporates single negative materials, Eur. Phys. J. D 71 (1) (2017) 11.
[21] Y.O. Averkov, Y.V. Prokopenko, V.M. Yakovenko, Eigenwave spectra of an anisotropic cylindrical solid-state waveguide, Tech. Phys. 64 (1) (2019) 1–7.
[22] T. Goto, A.V. Baryshev, M. Inoue, A.V. Dorofeenko, A.M. Merzlikin, A. P. Vinogradov, A.A. Lisyansky, A.B. Granovsky, Tailoring surfaces of one-dimensional magnetophotonic crystals: optical Tamm state and Faraday rotation, Am. Phys. Soc. B 79 (12) (2009) 125103.
[23] I.V. Treshin, V.V. Klimov, P.N. Melentiev, V.I. Balykin, Optical Tamm state and extraordinary light transmission through nanoaperture, Phys. Rev. 88 (2) (2013), 23832-23832.
[24] Y.H. Wu, F. Cheng, Y.C. Shen, G.Q. Lu, L.L. Li, One-way transmission through merging of magnetic defect state and optical Tamm states, Optik-Int. J. Light Electron Optic. 127 (8) (2016) 3740–3744.

[25] S. Chen, Dual-mode near-infrared light tunable absorber based on graphene by optical Tamm state and microcavity, Opt Commun. 492 (3) (2021) 126962.
[26] A. Kavokin, I. Shelykh, G. Malpuech, Optical Tamm states for the fabrication of polariton lasers, Appl. Phys. Lett. 87 (26) (2005) 193.
[27] W. Bo, Y. Zou, J. Wang, Novel electrical properties and applications in kaleidoscopic graphene nanoribbons, RSC Adv. 11 (2021).
[28] J.P. Lee-Thorp, M.I. Weinstein, Y. Zhu, Elliptic operators with honeycomb symmetry: Dirac points, edge states and applications to photonic graphene, Arch. Ration. Mech. Anal. 232 (1) (2019) 1–63.
[29] S.A. Mikhailov, K. Ziegler, A new electromagnetic mode in graphene, Phys. Rev. Lett. 99 (1) (2007), 016803.
[30] H.T. Jiang, Z.L. Wang, Z.G. Wang, H. Chen, Backward electronic Tamm states in graphene-based heterostructures, Phys. Lett. 375 (6) (2011) 1014–1018.
[31] G. Eda, G. Fanchini, M. Chhowalla, Large-area ultrathin films of reduced graphene oxide as a transparent and flexible electronic material, Nat. Nanotechnol. 3 (2008) 270–274.
[32] K.S. Novoselov, A.K. Geim, S.V. Morozov, D. Jiang, M.I. Katsnelson, I. V. Grigorieva, S.V. Dubonos, A.A. Firsov, Two-dimensional gas of massless Dirac fermions in graphene, Nature 438 (2005) 197–200.
[33] Y. Ma, T. Zhang, M. Mao, D. Zhang, H.F. Zhang, Switchable multifunctional modulator realized by the stacked graphene-based hyperbolic metamaterial unit cells, Opt Express 28 26 (2020).